Journal of Thermal Analysis and Calorimetry (2019) 135:671–683
https://doi.org/10.1007/s10973-018-7181-3

Numerical evaluation on thermal–hydraulic characteristics of dilute heat-dissipating nanofluids flow in microchannels

Comparison of different models

Mostafa Keshavarz Moraveji[1] · Ramtin Barzegarian[2] · Mehdi Bahiraei[3] · Matin Barzegarian[4] · Alireza Aloueyan[5] · Somchai Wongwises[6]

Received: 31 January 2018 / Accepted: 8 March 2018 / Published online: 15 March 2018

Abstract
The present work deals with numerical investigations on heat transfer characteristics and friction factor of aqueous CuO nanofluids flow in a set of four microchannels connected in parallel under laminar regime. For each single phase, volume of fluid, mixture and Eulerian models, a particular computer code is developed to carefully simulate this problem. The three-dimensional steady-state governing equations are solved through finite volume method. The primary aim of this study is to comparatively distinguish the most appropriate and accurate model for numerical studies of nanofluids in microchannels. The results are compared with one another and the data obtained from an experimental work. Regarding the results, an acceptable consistency is observed for all models with the experimental data. The current study truly demonstrates that applying single-phase model to simulate and evaluate the laminar flow of CuO–water nanofluid inside microchannels with uniform wall temperature is more modest, precise and reliable compared with two-phase models.

Keywords Laminar · Microchannel · Single-phase model · Two-phase models · Nanofluid · CFD

List of symbols

A	Heat transfer surface (m^2)
a	Acceleration (m s^{-2})
h	Convective heat transfer coefficient (W m^{-2} K^{-1})
C_d	Drag coefficient
d_p	Nanoparticle diameter (m)
C_p	Specific heat (J Kg^{-1} K^{-1})
k	Thermal conductivity (W m^{-1} K^{-1})
F	Force (N)
F_d	Drag force (Pa m^{-1})
F_{vm}	Virtual mass force (Pa m^{-1})
f	Friction factor
f_{drag}	Drag function
g	Gravity acceleration (m s^{-2})
h_v	Volumetric heat transfer coefficient (W m^{-3} K^{-1})
D_H	Hydrodynamic diameter (m)
h_p	Liquid-particle heat transfer coefficient (W m^{-2} K^{-1})
L	Channel length (m)
Nu	Average Nusselt number (hD/k)
P	Pressure (pa)
Pr	Prandtl number ($C_p\mu/k$)
Re	Reynolds number ($\rho UD/\mu$)
T	Temperature (K)
V	Velocity (m s^{-1})
Kn	Knudsen number

✉ Mostafa Keshavarz Moraveji
moraveji@aut.ac.ir

[1] Department of Chemical Engineering, Amirkabir University of Technology (Tehran Polytechnic), Tehran 15875-4413, Iran

[2] Department of Mechanical Engineering, Science and Research Branch, Islamic Azad University, Tehran, Iran

[3] Department of Mechanical Engineering, Kermanshah University of Technology, Kermanshah, Iran

[4] Department of Mechanical Engineering, West Tehran Branch, Islamic Azad University, Tehran, Iran

[5] Department of Mechanical Engineering, South Tehran Branch, Islamic Azad University, Tehran, Iran

[6] Fluid Mechanics, Thermal Engineering and Multiphase Flow Research Laboratory (FUTURE), Department of Mechanical Engineering, Faculty of Engineering, King Mongkut's University of Technology Thonburi, Bangmod, Bangkok 10140, Thailand

Greek symbols

μ Fluid dynamic viscosity (kg m^{-1} s^{-1})
ρ Mass density (kg m^{-3})
φ Volume concentration
β Friction coefficient (kg m^{-3} s^{-1})
α Thermal diffusivity (m^2 s^{-1})
η Viscosity (Pa s)

Subscripts

b Bulk
dr Drift
eff Effective
h Hot
f Base fluid
m Mixture
f Fluid
nf Nanofluid
p Nanoparticles
w Wall

Introduction

Over the past decade, computers and other modern electronic devices have been becoming far more widespread. Due to high heat generation of such devices, designing more efficient systems to dissipate away this heat in order to prevent overheating as well as chip failures is inevitable for industrial corporations. In comparison with voluminous traditional heat sinks, using liquid combined with micro- or mini-channels for cooling is more efficient and rational. Reducing the channel diameter leads to a higher heat transfer coefficient in consequence of a large surface area-to-volume ratio and also it augments heat conduction through the channel walls. Despite the positive points of microchannels, several disadvantages can also be considered including higher pressure drop due to the dimensions reduction and increment of the production costs. As another defect, fouling of fluid should also be taken into account. In spite of the mentioned cons, employing microchannels is still the most effectual and prevalent method of cooling electronic components.

For the first time in 1995, Choi [1] offered nanofluids which are engineered by adding and dispersing nanoscale metallic, metallic oxide, carbon or composite particles in conventional working fluids (water, ethylene glycol and mineral oils) as an innovative way of improving thermophysical properties of ordinary fluids and total heat transfer rate as a consequence. Nanofluids as novel agents for development of energy sustainability have incomparable potential to be employed as working fluid in a wide variety of thermal applications [2–13] such as heat pipes [14–17], heat exchangers [18–21], solar energy systems [22–25], refrigeration systems [26–31], engine cooling system [32–34], heat sinks [35–38] and so forth. Since the size of the solid particles is pretty small (1–100 nm), they perform identical as liquid molecules and flow smoothly through the microchannels. In recent years, utilizing microchannels operated with nanofluids for cooling purposes has become as an interesting topic of research for many scholars [39–46].

Nguyen et al. [47] experimentally analyzed the effect of water-based Al_2O_3 nanofluids on heat transfer characteristics of a closed electronic cooling system. They reported that heat transfer coefficient of nanofluid at 6.8% vol. nanoparticles enhances more than 40% compared to that of the base fluid. According to their observations about particle size effect, nanofluid with 36-nm particle size provides higher convective heat transfer coefficient rather than with 47-nm particle size.

An experimental investigation on performance of microchannel heat sink using CuO–water nanofluids as coolant was carried out by Chein and Chuang [48]. They observed a significant enhancement in the absorbed energy and a slight increase in pressure drop of the system utilizing nanofluids compared with the pure water.

Performing an experimental study on convective performance of Al_2O_3/DI–water nanofluids in a commercial electronics cooling system, Roberts and Walker [49] found an increment in convective heat transfer through using nanofluid at up to 1.5% vol. nanoparticles.

In another investigation, Khodabandeh and Abbassi [50] numerically calculated the optimum geometry for a trapezoidal microchannel with aqueous Al_2O_3 nanofluid flow using the two-phase Eulerian–Lagrangian model and constructal theory. Based on their findings, for an unchanged pressure drop, microchannel with side angle of 70° has the highest overall non-dimensional conductivity compared to others. Also they reported that the maximum thermal conductivity is reached for nanoparticle volume fraction ranging from 0.4 to 0.5%.

Ho et al. [51] conducted an experimental evaluation on hydraulic and thermal performance of a microchannel heat sink employing aqueous Al_2O_3 nanofluid. As mentioned in their paper, using nanofluids instead of pure water leads to a low increment in friction factor. By doing so, they also reported a remarkable enhancement in the average heat transfer coefficient. For instance, at 1% vol. nanoparticles, the average heat transfer coefficient rises around 70% compared to that of water.

Jang and Choi [52] examined the cooling performance of a microchannel heat sink utilizing diamond–H_2O nanofluid numerically. Based on their results, 10% enhancement in performance was observed through using the nanofluid at 1% volume loading of nanoparticles.

In another research, Kalteh et al. [53] studied the laminar forced convection of water-based Al_2O_3 nanofluids

flow inside a microchannel heat sink both experimentally and numerically. Homogenous and two-phase Eulerian–Eulerian methods were implemented to computationally determine the nanofluids forced convection. Regarding their comparative results, it is concluded that the results based on two-phase approach are in a better agreement with the experimental data. Furthermore, the mean Nusselt number increases as Reynolds number and nanoparticles volume concentration enhance. Eventually, they reported that average Nusselt number is strongly affected by nanoparticle size, insofar as the Nusselt number augments with decrement of particle size.

In this study, a numerical simulation on heat transfer characteristics and friction factor of dissipative nanofluids (CuO–water) flow in microchannels using FVM method is carried out based on an experimental investigation performed by Byrne et al. [54]. This experimental study was conducted on water-based CuO nanofluids with and without suspension enhancer (surfactant) flow through a combination of four parallel microchannels. Dimensions and assembly details of the microchannels test section are represented in Fig. 1a, b, respectively. The numerical simulation results are compared with the experimental data for nanofluids without surfactant. Nanofluids flow in microchannels at three various volume loadings (φ = 0.005, 0.01 and 0.1% vol.) is modeled. The main objective of the present work is to compare the experimental data with numerical results obtained using single-phase and two-phase models (VOF, Eulerian and mixture) in order to choose the most precise and reliable model for numerical studies of microchannels. Finally, some correlations for prediction of average Nusselt number and friction factor in microchannels are generated on the basis of the most accurate model. For each model, a particular computer code is developed to fulfill this purpose. The reliability of the codes was proven in a previous study by our team [55].

Numerical analysis

In this work, three-dimensional (3D) computational fluid dynamics (CFD) is considered for modeling and solving the problem. As previously mentioned, an individual code is separately developed for each four models. As shown in Fig. 2, for the current problem a computational domain with 6 mm length, 0.1 mm width and 0.119 mm depth has been defined. Steady-state fully developed laminar flow of CuO–water (nanoparticle size = 30–50 nm) nanofluids passes through the block.

Single-phase model

Nanofluid is considered as a homogenous fluid in the single-phase model. For the fluids with solid particles inclusion, Knudsen number (Kn) is defined as the molecular mean free path of the base liquid to the particles diameter [56]. Since the value of Kn number is found far less than 1 in the present study, the continuum assumption of fluid mechanics is authentic for the single-phase simulation model. Therefore, continuity, momentum and energy equations (governing equations) are written as [57]:

Continuity equation:

$$\nabla \cdot (\rho_{\mathrm{nf}} \cdot V_{\mathrm{m}}) = 0 \tag{1}$$

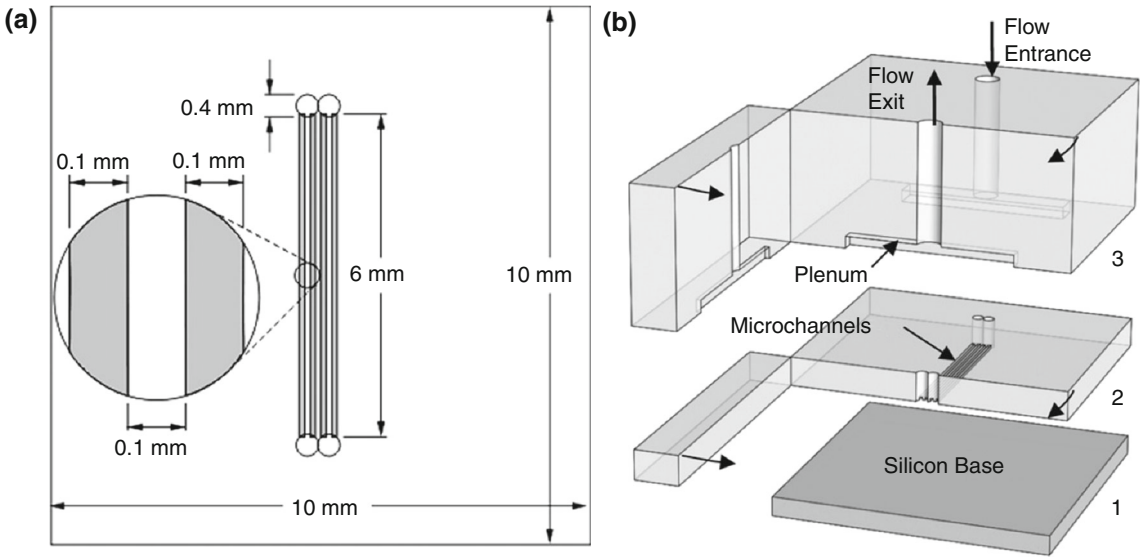

Fig. 1 Schematic of the microchannel test section: **a** test section dimensions and **b** test section assembly details. Layers (2) and (3) are fabricated as single pieces, but are shown in a sectioned view to illustrate interior details [54]. Reprinted with permission from Elsevier

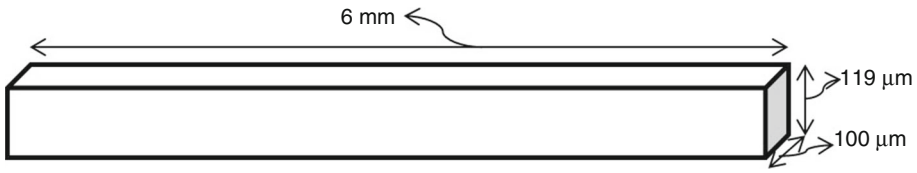

Fig. 2 Schematic of the numerical domain for this study

Momentum equation:

$$\nabla \cdot (\rho_{nf} \cdot V_m \cdot V_M) = -\nabla P + \nabla \cdot (\mu_{nf} \cdot \nabla V_m) \quad (2)$$

Energy equation:

$$\nabla \cdot (\rho_{nf} \cdot C \cdot V_m \cdot T) = \nabla \cdot (k_{nf} \cdot \nabla T) \quad (3)$$

The fluid is considered as a single continuous phase; hence, the following equations can be utilized to determine thermophysical properties of the nanofluid [58]:

$$\rho_{nf} = (1-\varphi)\rho_f + \varphi\rho_p \quad (4)$$

$$C_{pnf} = (1-\varphi)C_{pf} + \varphi C_{pp} \quad (5)$$

where ρ is density, C_p is specific heat capacity and φ is the volume concentration of nanoparticles. Also, *nf*, *f* and *p* subscripts refer to nanofluid, base fluid and nanoparticles, respectively.

The following correlation can be used to determine the viscosity of the nanofluids [59]:

$$\mu_{nf} = \mu_f \left(\frac{1}{(1-\varphi)^{2.5}} \right) \quad (6)$$

The effective thermal conductivity of the nanofluid is defined as [60]:

$$\frac{k_{nf}}{k_f} = 1 + 64.7\phi^{0.7640} \left(\frac{d_f}{d_p} \right)^{0.3690} \left(\frac{k_f}{k_p} \right)^{0.7476} Pr_T^{0.9955} Re_T^{1.2321} \quad (7)$$

where Pr_T and Re_T are defined as:

$$Pr_T = \frac{\mu_f}{\rho_f \alpha_f} \quad (8)$$

$$Re_T = \frac{\rho_f k_b T}{3\pi\mu_f^2 l_f} \quad (9)$$

where k_b is the Boltzmann constant which is equal to 1.3807×10^{-23} *J*/K and l_f is the mean free path of fluid particles (= 0.17 nm) [60]. In this model, the effects of nanoparticle size and temperature at the temperature range between 21 and 70 °C are considered.

Two-phase models

Mixture model

Indeed, the mixture model considers the fluid as a mixture of dispersed and continuous phases. The mixture model is the most suitable option to simulate and investigate the bubbles in fluids as well as liquids with small particles inclusion [61]. For this model, the governing equations are analogously written to the homogeneous model. By balancing both the body and drag forces due to density variations, slip of a dispersed phase relative to the continuous phase could be truly determined. Local equilibrium as a fundamental supposition is considered in the mixture model. According to this assumption, the suspended particles travel evermore with their terminal velocity corresponding to the continuous phase. Until the force equilibrium is attained, the mixture model could be employed for a wide range of particle size, velocity variations and density ratios.

The steady-state governing equations (continuity, momentum and energy) are defined as [62]:

Continuity equation:

$$\nabla \cdot (\rho_m \cdot V_m) = 0 \quad (10)$$

Momentum equation:

$$\nabla \cdot (\rho_m \cdot V_m \cdot V_m) = -\nabla P + \nabla \cdot (\mu_m \cdot \nabla V_m) + \nabla \cdot \left(\sum_{k=1}^{n} \phi_k \rho_k V_{dr,k} V_{dr,k} \right) - \rho_{m,i} \beta_m g (T - T_i) \quad (11)$$

where ρ_m and μ_m as the mixture density and viscosity are generally defined as:

$$\rho_m = \sum_{k=1}^{n} \phi_k \rho_k \quad (12)$$

$$\mu_m = \sum_{k=1}^{n} \phi_k \mu_k \quad (13)$$

where ϕ_k is the volume fraction of phase *k* and $\sum_{k=1}^{n} \phi_k = 1$.

Energy equation:

$$\nabla \cdot \sum_{k=1}^{n} (\rho_k \cdot C_{pk} \cdot \phi_k \cdot V_k \cdot T) = \nabla \cdot (\lambda_m \cdot \nabla T) \quad (14)$$

where λ_m as the mixture thermal conductivity is:

$$\lambda_m = \sum_{k=1}^{n} \phi_k \lambda_k \quad (15)$$

Volume fraction equation:

$$\nabla \cdot \left(\phi_{\mathrm{p}} \rho_{\mathrm{p}} V_{\mathrm{m}}\right) = -\nabla \cdot \left(\phi_{\mathrm{p}} \rho_{\mathrm{p}} V_{\mathrm{dr,p}}\right) \tag{16}$$

where V_{m} is mass average velocity:

$$V_{\mathrm{m}} = \frac{\sum_{k=1}^{n} \phi_{\mathrm{k}} \rho_{\mathrm{k}} V_{\mathrm{dr,k}}}{\rho_{\mathrm{m}}} \tag{17}$$

$V_{\mathrm{dr,k}}$ as the drift velocity for the secondary phase k (nanoparticle) can be determined through Eq. (18):

$$V_{\mathrm{dr,k}} = V_{\mathrm{pf}} - \sum_{i=1}^{n} \frac{\phi_{\mathrm{k}} \rho_{\mathrm{k}}}{\rho_{\mathrm{m}}} V_{\mathrm{fk}} \tag{18}$$

The following correlations are used to determine V_{pf} (slip velocity):

$$V_{\mathrm{pf}} = V_{\mathrm{p}} - V_{\mathrm{f}} \tag{19}$$

$$V_{\mathrm{pf}} = \frac{\rho_{\mathrm{p}} d_{\mathrm{p}}^2}{18 \mu_{\mathrm{f}} f_{\mathrm{drag}}} \frac{\left(\rho_{\mathrm{p}} - \rho_{\mathrm{m}}\right)}{\rho_{\mathrm{p}}} a \tag{20}$$

$$f_{\mathrm{drag}} = f(x) = \begin{cases} 1 + 0.15 \mathrm{Re}_{\mathrm{p}}^{0.687} \text{ for } \mathrm{Re}_{\mathrm{p}} \leq 1000 \\ 0.0183 \ \mathrm{Re}_{\mathrm{p}} \text{ for } \mathrm{Re}_{\mathrm{p}} > 1000 \end{cases} \tag{21}$$

The subscripts p and f correspond to secondary phase (nanoparticle) and primary phase (water) of the fluid, respectively.

The acceleration in Eq. (20) is defined as:

$$a = g - (V_{\mathrm{m}} \cdot \nabla) V_{\mathrm{m}} \tag{22}$$

Eulerian model

Continuity, momentum and energy equations are separately solved for each phase in the Eulerian model as another multiphase model. For each phase, a set of equations is characterized by volume fractions. Comparing with the mixture model, Eulerian model is far more difficult to use due to powerful coupling. Eulerian model is also applicable for a wide range of volume (dilute to dense) and particle (low to high) loadings as well. For both particle and base fluid phases, the governing equations (mass, momentum and energy) can be presented as [53]:

$$\nabla \cdot \left(\rho_{\mathrm{l}} \varphi_{\mathrm{l}} \vec{V}_{\mathrm{l}}\right) = 0 \tag{23}$$

$$\nabla \cdot \left(\rho_{\mathrm{p}} \varphi_{\mathrm{p}} \vec{V}_{\mathrm{p}}\right) = 0 \tag{24}$$

$$\varphi_{\mathrm{l}} + \varphi_{\mathrm{p}} = 1 \tag{25}$$

$$\nabla \cdot \left(\rho_{\mathrm{l}} \varphi_{\mathrm{l}} \vec{V}_{\mathrm{l}} \vec{V}_{\mathrm{l}}\right) = -\varphi_{l} \nabla p + \nabla \cdot \left[\varphi_{\mathrm{l}} \mu_{\mathrm{l}} \left(\nabla \vec{V}_{\mathrm{l}} + \nabla \vec{V}_{\mathrm{l}}^{\mathrm{T}}\right)\right] + F_{\mathrm{d}} + F_{vm} \tag{26}$$

$$\nabla \cdot \left(\rho_{\mathrm{p}} \varphi_{\mathrm{p}} \vec{V}_{\mathrm{p}} \vec{V}_{\mathrm{p}}\right) = -\varphi_{\mathrm{p}} \nabla p + \nabla \cdot \left[\varphi_{\mathrm{p}} \mu_{\mathrm{p}} \left(\nabla \vec{V}_{\mathrm{p}} + \nabla \vec{V}_{\mathrm{p}}^{T}\right)\right] - F_{\mathrm{d}} + F_{V\mathrm{m}} + F_{\mathrm{col}} \tag{27}$$

In the current study, the lift force could be neglected due to the very small size (in nanometer-sized) of the particles. Only the drag force between the phases (F_{d}) must be taken into consideration as follows:

$$F_{\mathrm{d}} = -\beta \left(\vec{V}_{\mathrm{l}} - \vec{V}_{\mathrm{p}}\right) \tag{28}$$

β (friction coefficient) is calculated on the basis of volume fraction range and its value for a very dilute two-phase flow with particle diameter d_{p} can be determined as:

$$\beta = \frac{3}{4} C_{\mathrm{d}} \frac{\varphi_{\mathrm{l}} (1 - \varphi_{\mathrm{l}})}{d_{\mathrm{p}}} \rho_{\mathrm{l}} \left|\vec{V}_{\mathrm{l}} - \vec{V}_{\mathrm{p}}\right| \varphi_{\mathrm{l}}^{-2.65} \tag{29}$$

Equation (27) is authentic for two-phase flows including particles in more than 0.8 volume fractions. The drag coefficient (C_{d}) magnitude relies on the particle Reynolds number as:

$$C_{\mathrm{d}} = \begin{cases} \frac{24}{\mathrm{Re}_{\mathrm{p}}} \left(1 + 0.15 \mathrm{Re}_{\mathrm{p}}^{0.687}\right) \text{ for } \mathrm{Re}_{\mathrm{p}} < 1000 \\ 0.44 \text{ for } \mathrm{Re}_{\mathrm{p}} \geq 1000 \end{cases} \tag{30}$$

where

$$\mathrm{Re}_{\mathrm{p}} = \frac{\varphi_{\mathrm{l}} \rho_{\mathrm{l}} \left|\vec{V}_{\mathrm{l}} - \vec{V}_{\mathrm{p}}\right| d_{\mathrm{p}}}{\mu_{\mathrm{l}}} \tag{31}$$

Negligence of the viscous dissipation and radiation and assuming the base liquid and the nanoparticle phases as incompressible fluids as well, the energy equation can be rewritten as follows:

$$\nabla \cdot \left(\rho_{\mathrm{l}} \varphi_{\mathrm{l}} C_{\mathrm{pl}} T_{\mathrm{l}} \vec{V}_{\mathrm{l}}\right) = \nabla \cdot \left(\varphi_{\mathrm{l}} k_{\mathrm{eff,l}} \nabla T_{\mathrm{l}}\right) - h_{v} \left(T_{\mathrm{l}} - T_{\mathrm{p}}\right) \tag{32}$$

$$\nabla \cdot \left(\rho_{\mathrm{p}} \varphi_{\mathrm{p}} C_{\mathrm{pp}} T_{\mathrm{p}} \vec{V}_{\mathrm{p}}\right) = \nabla \cdot \left(\varphi_{\mathrm{p}} k_{\mathrm{eff,p}} \nabla T_{\mathrm{p}}\right) + h_{v} \left(T_{\mathrm{l}} - T_{\mathrm{p}}\right) \tag{33}$$

For monodispersed spherical particles, h_{v} can be obtained from the following correlation:

$$h_{v} = \frac{6(1 - \varphi_{\mathrm{l}})}{d_{\mathrm{p}}} h_{\mathrm{p}} \tag{34}$$

where h_{p} as the fluid–particle heat transfer coefficient can be determined based on the experimental correlations available in the literature. An empirical correlation developed by Wakao and Kaguei [63] is used to calculate the fluid–particle heat transfer coefficient in the current study as follows:

$$\mathrm{Nu}_{\mathrm{p}} = \frac{h_{\mathrm{p}} d_{\mathrm{p}}}{k_{\mathrm{l}}} = 2 + 1.1 \mathrm{Re}_{\mathrm{p}}^{0.6} \mathrm{Pr}^{1/3} \tag{35}$$

For liquid and particle phases, the effective thermal conductivity is determined as:

$$k_{\mathrm{eff,l}} = \frac{k_{\mathrm{b,l}}}{\varphi_{\mathrm{l}}} \tag{36}$$

$$k_{\mathrm{eff,p}} = \frac{k_{\mathrm{b,p}}}{\varphi_{\mathrm{p}}} \tag{37}$$

where

$$k_{\mathrm{b,l}} = \left(1 - \sqrt{(1-\varphi_{\mathrm{l}})}\right) k_{\mathrm{l}} \tag{38}$$

$$k_{\mathrm{b,p}} = \sqrt{(1-\varphi_{\mathrm{l}})}(\omega A + [1-\omega]\Gamma) k_{\mathrm{l}} \tag{39}$$

and

$$\Gamma = \frac{2}{\left(1-\frac{B}{A}\right)} \left\{ \frac{B(A-1)}{A\left(1-\frac{B}{A}\right)^2} \ln\left(\frac{A}{B}\right) - \frac{(B-1)}{\left(1-\frac{B}{A}\right)} - \frac{B+1}{2} \right\} \tag{40}$$

with

$$B = 1.25\left(\frac{[1-\varphi_{\mathrm{l}}]}{\varphi_{\mathrm{l}}}\right)^{10/9} \tag{41}$$

For spherical particles:

$$A = \frac{k_{\mathrm{p}}}{k_{\mathrm{l}}} \tag{42}$$

and

$$\omega = 7.26 \times 10^{-3} \tag{43}$$

VOF model

As other type of multiphase models, volume-of-fluid (VOF) model is a free-surface modeling method. Indeed, location of the liquid–liquid interface (free surface) is tracked in this model. For this purpose, a single momentum equation is solved throughout the fluid domain, and then, the achieved velocity field is shared among all phases. Eventually, a single energy equation is applied to calculate a shared temperature. It should be noted that the momentum and energy conservation equations in VOF model are presented as given in Eqs. (2) and (3), while continuity equation is individually presented as follows [64]:

$$\nabla \cdot (\varphi_{\mathrm{q}} \rho_{\mathrm{q}} \overrightarrow{V_{\mathrm{q}}}) = 0 \tag{44}$$

where $\sum_{q=1}^{n} \varphi_{\mathrm{q}} = 1$ and all properties are calculated alike $N = \sum_{q=1}^{n} \varphi_{\mathrm{q}} N_{\mathrm{q}}$ (n is number of the phases).

Boundary conditions

For solving the governing equations, the following boundary conditions are applied to all four models:

- Velocity:
  Inlet condition at the input face of the block (z = 0):
  $$\begin{cases} V_{\mathrm{x}} = V_{\mathrm{y}} = 0, V_{\mathrm{z}} = V_0 \\ \phi = \phi_0 \\ T = T_0 = 14\,^{\circ}\mathrm{C} \end{cases}$$
- Walls:
  No slip condition at the interface for the two side faces and upper and beneath faces of the block:
  $V_{\mathrm{x}} = V_{\mathrm{y}} = V_{\mathrm{z}} = 0$

  For the beneath face of the block (constant temperature):
  $T = T_{\mathrm{i}} = 24\,^{\circ}\mathrm{C}$

  For two side faces and upper face of the block (thermal insulation):
  $-k_{\mathrm{nf}} \nabla \mathrm{T} = 0$
- Pressure:
  No viscous stress condition at outlet face of the block (z = L):
  The following overall mass balance correction is used:
  $P = P_0 = 0$

Numerical solution

The set of differential equations are discretized through FVM (finite volume method) and solved iteratively applying the line-by-line technique as well. For the convective and diffusive terms, the second-order upwind method is utilized, while for the velocity–pressure coupling, the SIMPLEC procedure is applied. For discretization, a structured non-uniform grid is employed which is closer to the blocks inlet and near beneath the wall where both temperature and velocity gradients are greater. The sum of scaled absolute residuals for all present parameters (velocity, mass and temperature) is limited to remain lower than 10^{-6} as criterion of convergence.

Grid independency and code validation

Three individual structured meshes are tested for each model to accurately investigate the independency of results from the number of grids. According to Fig. 3, for all four models the calculated mean Nusselt numbers do not show significant change after applying the 600 × 20 × 10 grids comparing to 300 × 10 × 5 grids. So, the 300 × 10 × 5 grids (length × depth × width) are opted for this numerical simulation. In addition, the calculated average Nusselt numbers for pure water are compared with those

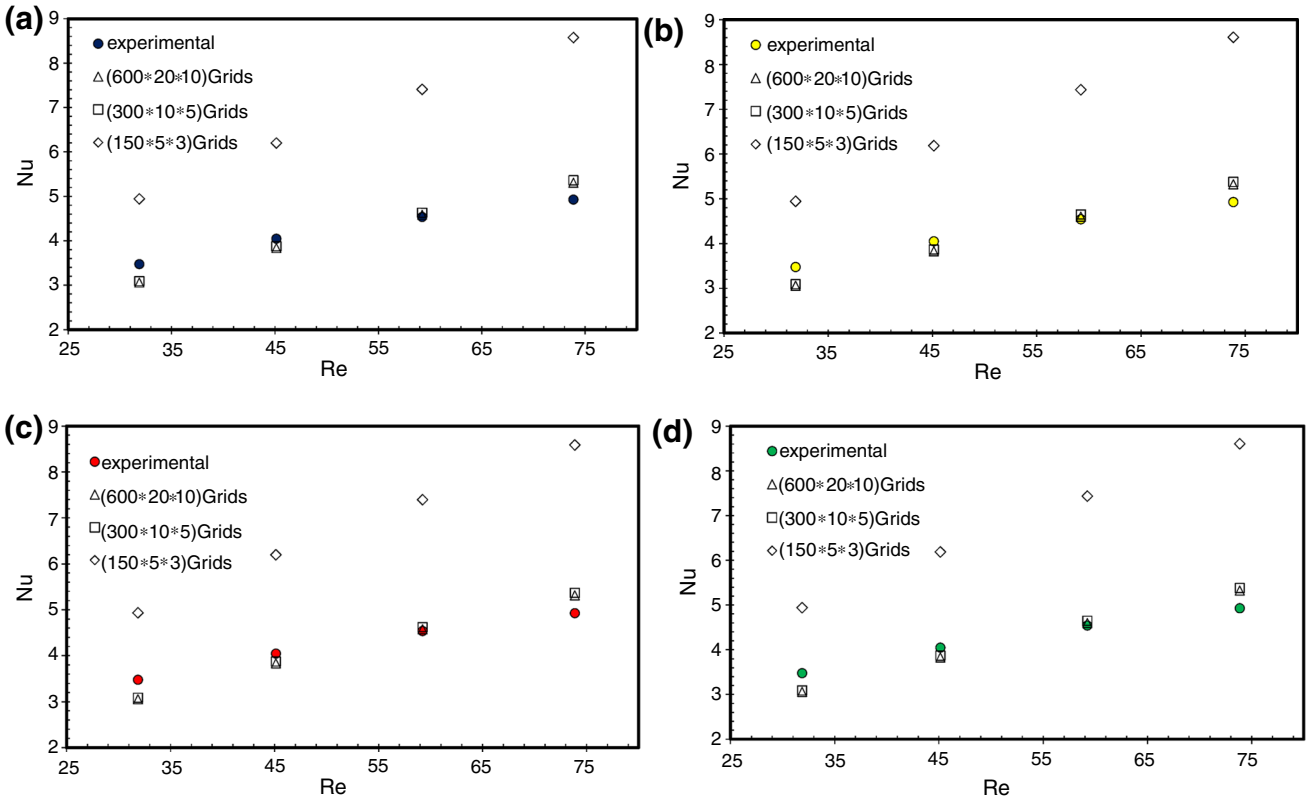

Fig. 3 Grid independency and code validation with average Nusselt number (four microchannels) for pure water flow (**a**: single phase, **b**: Eulerian model, **c**: VOF model, **d**: mixture model)

determined experimentally [54] in order to evaluate the computer codes. The highest deflection from the experimental data for the single-phase model is approximately 12%, and for Eulerian, mixture and VOF models are specified about 11% as well.

Calculation of thermal–hydraulic characteristics

Average nusselt number

Four parallel microchannels were used in the experiment by Byrne et al. [54]. To calculate the average Nusselt number, the following equations are used as follows:

$$q = \dot{m} C_{\mathrm{Pnf}} (T_{\mathrm{out}} - T_{\mathrm{in}}) \tag{45}$$

$$D_{\mathrm{H}} = \frac{4W \cdot H}{2(W + H)} \tag{46}$$

$$A = L \times W \tag{47}$$

$$\mathrm{Nu} = \frac{q \cdot D_{\mathrm{H}}}{4Ak_{\mathrm{nf}}(T_{\mathrm{W}} - T_{\mathrm{b}})} \tag{48}$$

where D_{H}, q, $\dot{m}$, W, H, L, T_{in}, T_{out}, T_{w}, and T_{b} are the hydrodynamic diameter, total heat transfer, total mass flow rate, width, height (depth), length, inlet temperature, outlet temperature, wall temperature (beneath the block) and bulk temperature, respectively.

For converting the total mass flow rate to dimensionless Reynolds number:

$$u = \frac{\dot{m}}{4\rho_{\mathrm{nf}} A} \tag{49}$$

$$\mathrm{Re} = \frac{\rho_{\mathrm{nf}} u D_{\mathrm{H}}}{\mu_{\mathrm{nf}}} \tag{50}$$

Friction factor

For evaluating the friction factor, the following correlation is used [20]:

$$f = \frac{2 \cdot D_{\mathrm{H}} \cdot \Delta P}{\rho_{\mathrm{nf}} L u^2} \tag{51}$$

where ΔP is the total pressure drop.
Pumping power (P_{p}) is defined as:

$$P_{\mathrm{p}} = \dot{V}_{\mathrm{nf}} \Delta P \tag{52}$$

where $\dot{V}_{\mathrm{nf}}$ is volume flow rate of the nanofluid.

Results and discussion

Average nusselt number

All applied geometry, volume fractions and boundary conditions for the current simulation are identical to the experiments performed by Byrne et al. [54]. The first test section of the experimental work and the case with no suspension enhancer was chosen to be simulated and intently compared. Figure 4 illustrates the comparison of the average Nusselt number obtained numerically with the experimental data [54]. According to Fig. 4, at $\varphi = 0.005\%$ almost the same results are achieved from the four models. As the volume loading increases to $\varphi = 0.01\%$, the single-phase model shows a better approximation of the experimental data comparing to the two-phase models. For the highest volume fraction (0.1% vol.), the deviation between the two-phase and single-phase models becomes more distinctive. The numerical results based on single-phase model are evidently in a better agreement with the experimental data. Relatively similar results are acquired using two-phase models (mixture, Eulerian and VOF) at all nanoparticle concentrations which overestimate the experimental data. This matter may be justified by the fact that the two-phase models are more sensitive to the presence of nanoparticles (changes in concentration) than the single-phase model. Maximum errors for the single phase, Eulerian, VOF and mixture models are specified around 9.14, 16.46, 17.05 and 17.04%, respectively. Although the effects of some physical phenomena such as gravity, drag, thermophoresis and Brownian motion are not directly considered in the single-phase model, this model yields far closer results to the experimental data compared with the two-phase models. It can be attributed to the fact that the effects of mentioned factors are taken into account in the single-phase simulations indirectly. In other words, because an experimental model has been adopted to determine thermal conductivity of the current nanofluids in the single-phase model, the influences of those factors exist in the model, which can affect the results of the simulation. Unlike imagination, it should be noted that the two-phase approaches include more simplifying assumptions in comparison with the single-phase method, which can cause some error in the

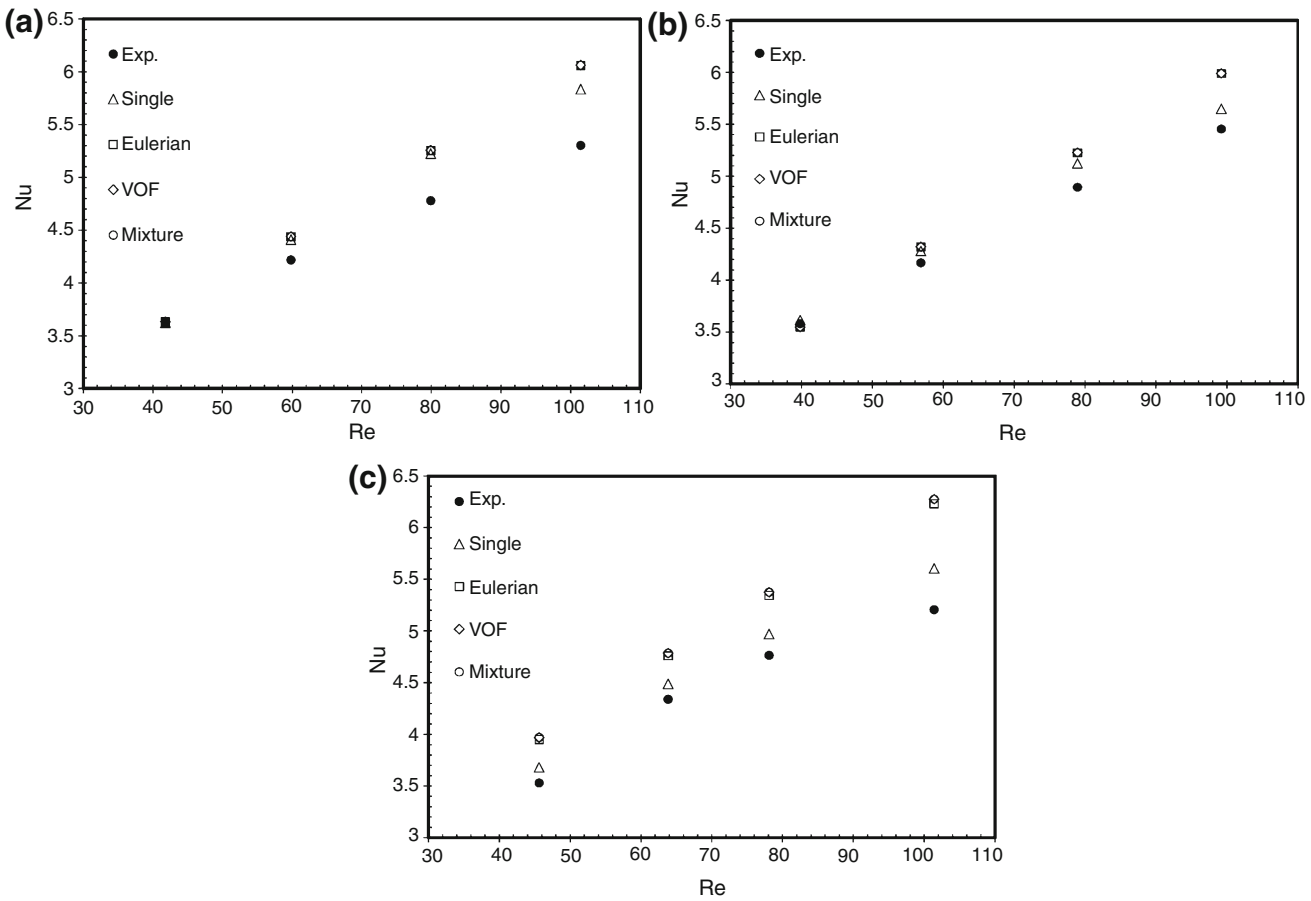

Fig. 4 Comparison between calculated average Nusselt numbers (four microchannels) with the experimental data by Byrne et al. [54]. (**a**: $\varphi = 0.005\%$, **b**: $\varphi = 0.01\%$, **c**: $\varphi = 0.1\%$)

results. Since the single-phase model gave the most precise outcomes of all, a correlation for average Nusselt number is developed based on its results:

$$\mathrm{Nu} = 0.3837\mathrm{Re}^{0.58}\,\mathrm{Pr}^{0.057}\,(1+\varphi)^{2.08} \tag{53}$$

$$\text{For} \begin{cases} 31.86 \le \mathrm{Re} \le 101.44 \\ 4.82 \le \mathrm{Pr} \le 7 \\ 0 \le \varphi \le 0.001 \end{cases}$$

This correlation could be applied for laminar flow of CuO–water nanofluid in microchannels on the above-mentioned validity range. Possible deviation of the average Nusselt number correlation from the results obtained through single-phase model is presented in Fig. 5.

Figure 6 illustrates the effect of adding nanoparticle on mean Nusselt number of the base liquid on the basis of the single-phase results. Apparently, increment of volume loading augments average Nusselt number of nanofluids at all velocities. Although the average Nusselt number of nanofluids at whole tested concentrations (0.005, 0.01 and 0.1% vol.) is very close to each other, they are all above that of pure water. Significant enhancements in Nusselt number are observed as the volume fraction increases to φ = 0.6 and 1%. For the nanofluid with a concentration of 1% by volume and v = 0.558 m/s, the Nusselt number rises approximately 50% in comparison with pure water at the same velocity. These enhancements in heat transfer of the base fluid with nanoparticle addition could be attributed to some feasible reasons, i.e., Brownian motion, friction force between the reference fluid and nanoparticles, particle-to-particle thermal interaction and energy exchange between the particles and the bulk fluid. Brownian motion as the random motion of nanoparticles within the bulk liquid principally affects the heat transfer enhancements. As another cause, dispersion of nanoparticles into the base liquid results in reduction of thermal boundary layer thickness which could intensify heat transfer improvement consequently.

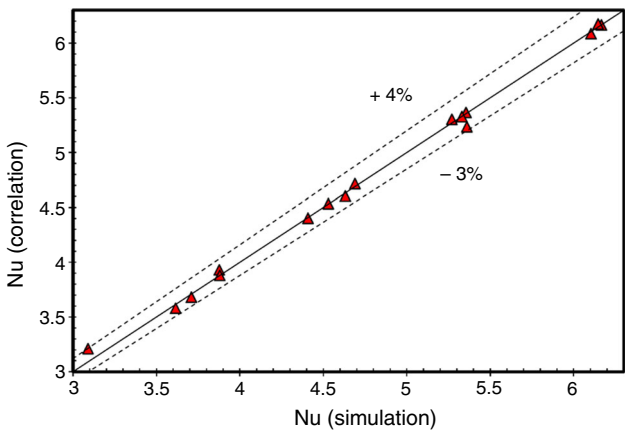

Fig. 5 Deviation between the Nusselt number correlation and the single-phase model results

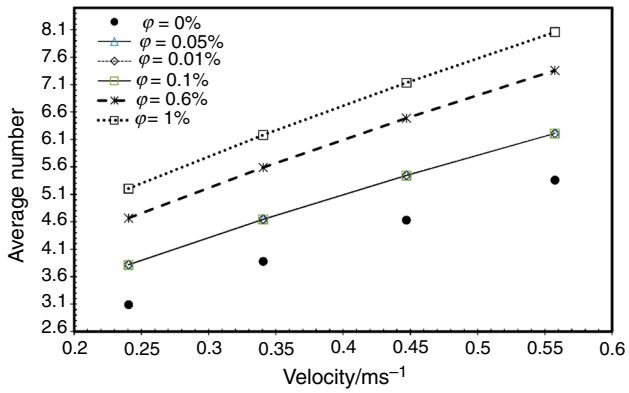

Fig. 6 Effect of nanoparticle volume fraction value on the average Nusselt number based on the single-phase model results (four microchannels)

Friction factor

Figure 7 comparatively demonstrates the friction factor results achieved by the mentioned numerical models and the experimental data as well. As shown in Fig. 7, a good match exists between experimental and numerical (entire models) results for friction factor. Compared to the experimental outcomes, applying all four computational models leads to the maximum deviance of up to 13%.

Due to the fact that the single-phase model takes less CPU usage and time to run compared to another models, a correlation on the basis of its results is generated for prediction of friction factor in microchannels:

$$f = 52.2\mathrm{Re}^{-0.97}(1+\varphi)^{11.16} \tag{54}$$

$$\text{For} \begin{cases} 31.86 \le \mathrm{Re} \le 101.44 \\ 0 \le \varphi \le 0.001 \end{cases}$$

Figure 8 shows the deviation of this correlation from the results based on single-phase model.

The effect of nanoparticle addition on pumping power is clearly depicted in Fig. 9. It is evident that despite no considerable change in pumping power by raising the volume fraction (φ) from 0 to 0.1%, fluid velocity (0.24–0.558 m s^{-1}) plays a significant role in determining its value. Figure 9 also shows the comparison of the calculated pumping power from the single-phase model with the experimental results.

In accordance with the equations indicated from this work, a prediction is made to specify the most appropriate value of nanoparticles volume fraction that corresponds with less pressure drop penalties in microchannels. Figure 10 depicts the variations of average Nusselt number and pressure drop of water-based CuO nanofluids as a function of nanoparticles volume fraction at v = 0.24 m s^{-1}. As can be

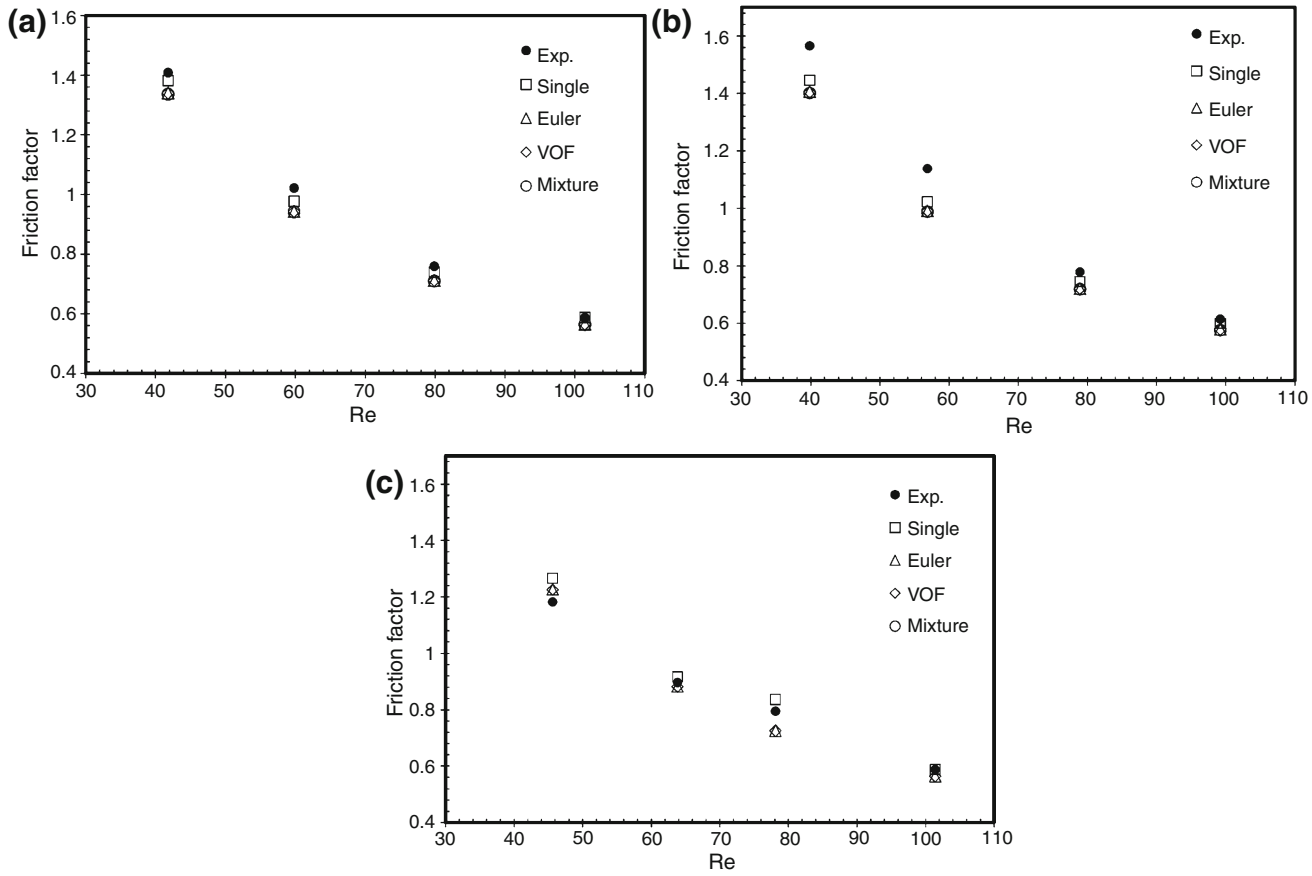

Fig. 7 Comparison between calculated friction factors (four microchannels) with the experimental data by Byrne et al. [54]. (**a**: $\varphi = 0.005\%$, **b**: $\varphi = 0.01\%$, **c**: $\varphi = 0.1\%$)

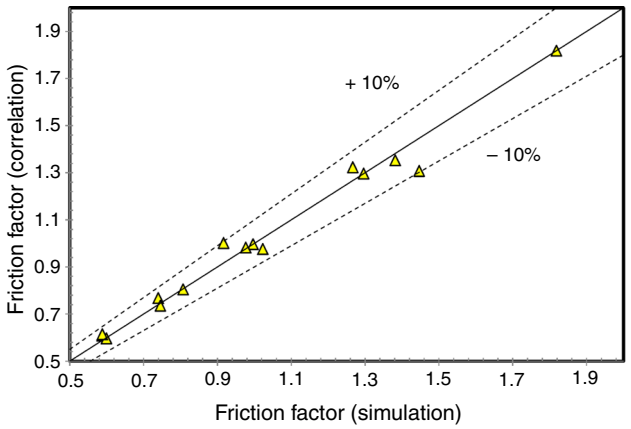

Fig. 8 Deviation between the friction factor correlation and the numerical (single-phase model) results

observed, although both pressure drop and Nusselt number possess the ascending trends in terms of volume fraction, there is an optimum point after which the pressure drop has the more significant values than the Nusselt number. In fact, for the volume loadings lower than 0.28%, the heat transfer is more noticeable compared with the pressure drop, and employing the nanofluid in this range could be optimal.

Conclusions

A 3D numerical study was conducted on the laminar flow of $CuO–H_2O$ nanofluid through a combination of four parallel microchannels. The problem was comprehensively simulated through applying a single-phase model and three particular two-phase models (mixture, Eulerian and VOF). Four individual computer codes were developed to fulfill this purpose.

In order to find the most appropriate model and to validate the codes as well, the numerical outcomes from each model were compared with the experimental data reported by Byrne et al. [54]. Comparing the experimental and computational results for both Nusselt number and friction factor, it is concluded that:

- All three two-phase models overestimated the experimental Nusselt number for all volume fractions. This may be attributed to the fact that the two-phase models

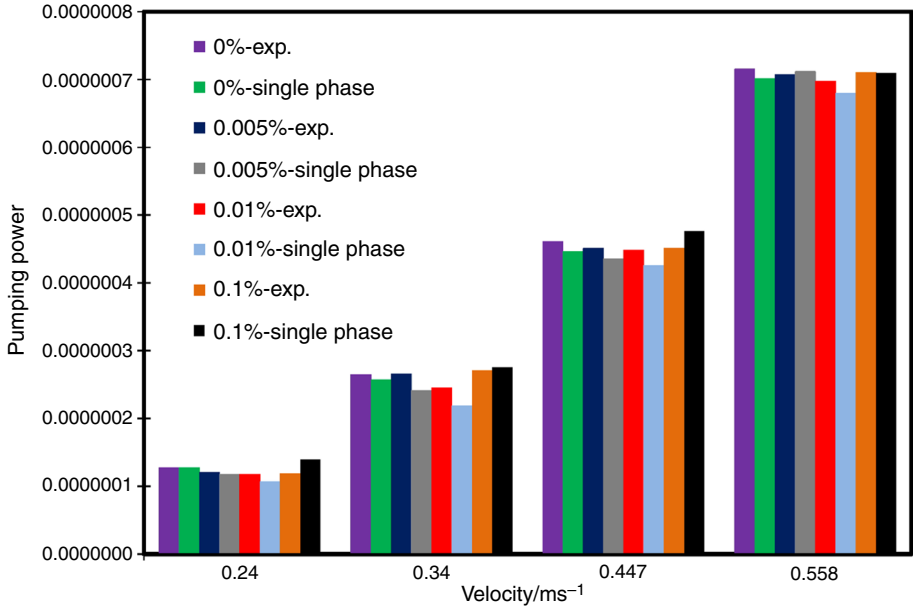

Fig. 9 Effect of nanoparticles volume fraction on pumping power (four microchannels)

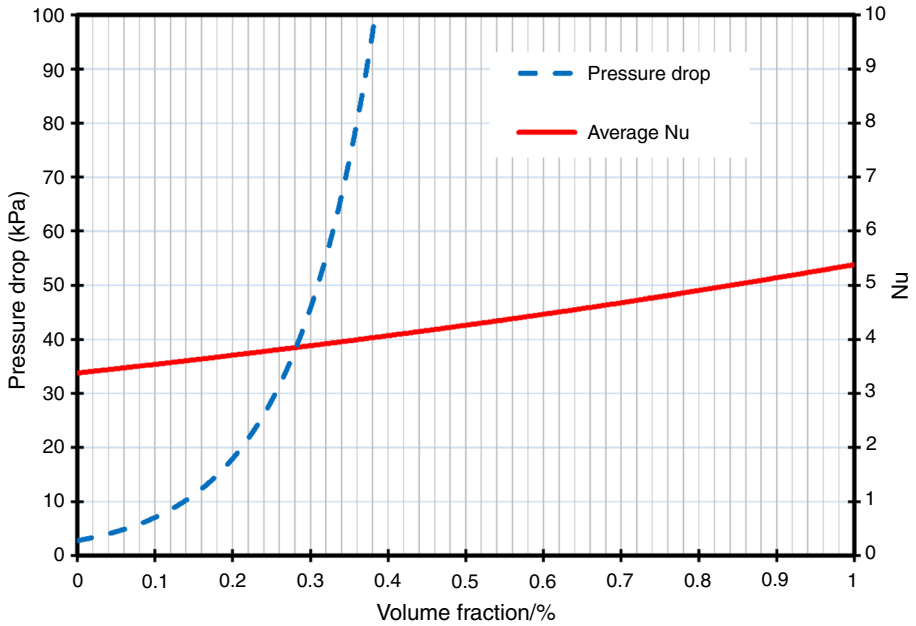

Fig. 10 Average Nusselt number and pressure drop of nanofluids (at $v = 0.24$ m/s) predicted based on the single-phase results (four microchannels)

are more sensitive to the volume concentration changes rather than single-phase model. Also, it was observed that the single-phase model yields closer results to the experimental data rather than the two-phase models. It may be corresponded to the fact that the effects of some physical forces, i.e., gravity, drag, Brownian and thermophoretic are considered in the single-phase simulations indirectly while they may be neglected through the two-phase approaches.

- The results based on single-phase model show a better consistency with the experimental Nusselt numbers at all fractions and also Reynolds numbers. Especially at higher volume fractions, it gives far closer results to the experimental data, compared with the two-phase models.
- With regard to the friction factor results, it could also be derived that as a whole the models show identical results for all concentrations. The maximum deviation of the simulated results from the experimental data does not exceed 13%.
- Since the single-phase model takes less CPU usage and time to run and give a more accurate approximation of the experimental data, the correlations for friction

factor and Nusselt number were generated on the basis of the single-phase model results.

- The single-phase model results confirmed the enhancement in the mean Nusselt number. Moreover, a graph was developed based on the correlations (this paper) to approximate the optimum volume fraction of nanoparticles which corresponds with less pressure drop penalties in microchannels.

The results from the present work demonstrate that using the single-phase model with complex property models to simulate and evaluate laminar aqueous CuO nanofluid flows in microchannels with uniform wall temperature is more careful and reliable rather than two-phase models.

References

1. Choi SUS. Enhancing thermal conductivity of fluids with nanoparticles. ASME-FED. 1994;231:99–105.
2. Mohammed H, Al-Aswadi A, Abu-Mulaweh H, Hussein AK, Kanna P. Mixed convection over a backward-facing step in a vertical duct using nanofluids-buoyancy opposing case. J Comput Theor Nanosci. 2014;11:1–13.
3. Ahmed S, Hussein AK, Mohammed H, Sivasankaran S. Boundary layer flow and heat transfer due to permeable stretching tube in the presence of heat source/sink utilizing nanofluids. Appl Math Comput. 2014;238:149–62.
4. Chand R, Rana G, Hussein AK. Effect of suspended particles on the onset of thermal convection in a nanofluid layer for more realistic boundary conditions. Int J Fluid Mech Res. 2015;42(5):375–90.
5. Chand R, Rana G, Hussein AK. On the onset of thermal Instability in a low Prandtl number nanofluid layer in a porous medium. J Appl Fluid Mech. 2015;8(2):265–72.
6. Dogonchi AS, Ganji DD. Investigation of MHD nanofluid flow and heat transfer in a stretching/shrinking convergent/divergent channel considering thermal radiation. J Mol Liq. 2016;220:592–603.
7. Mashayekhi R, Khodabandeh E, Bahiraei M, Bahrami L, Toghraie D, Akbari OA. Application of a novel conical strip insert to improve the efficacy of water–Ag nanofluid for utilization in thermal systems: a two-phase simulation. Energ Convers Manag. 2017;151:573–86.
8. Dogonchi A, Alizadeh M, Ganji D. Investigation of MHD go-water nanofluid flow and heat transfer in a porous channel in the presence of thermal radiation effect. Adv Powder Technol. 2017;28(7):1815–25.
9. Ahmadi AA, Khodabandeh E, Moghadasi H, et al. J Therm Anal Calorim. 2017. https://doi.org/10.1007/s10973-017-6798-y.
10. Arabpour A, Karimipour A, Toghraie D. J Therm Anal Calorim. 2018;131:1553. https://doi.org/10.1007/s10973-017-6649-x.
11. Hemmat Esfe M, Esfandeh S, Rejvani M. J Therm Anal Calorim. 2018;131:1437. https://doi.org/10.1007/s10973-017-6680-y.
12. Selimefendigil F, Chamkha AJ. J Therm Anal Calorim. 2018. https://doi.org/10.1007/s10973-018-7037-x.
13. Pourfayaz F, Sanjarian N, Kasaeian A, et al. J Therm Anal Calorim. 2018;131:1577. https://doi.org/10.1007/s10973-017-6500-4.
14. Moraveji MK, Razvarz S. Experimental investigation of aluminium oxide nanofluid on heat pipe thermal performance. Int Commun Heat Mass Transf. 2012;39:1444–8.
15. Vijayakumar M, Navaneethakrishnan P, Kumaresan G. Thermal characteristics studies on sintered wick heat pipe using CuO and Al_2O_3 nanofluids. Exp Therm Fluid Sci. 2016;79:25–35.
16. Sadeghinezhad E, Mehrali M, Rosen MA, Akhiani AR, Latibari ST, Mehrali M, Metselaar HSC. Experimental investigation of the effect of graphene nanofluids on heat pipe thermal performance. Appl Therm Eng. 2016;100:775–87.
17. Mohanraj C, Dineshkumar R, Muguran G, Experimental studies on effect of the heat transfer with Cuo-H_2O nanofluid on flat plate heat pipe. In: 5th International Conference of Materials Proc A. Characterization, ICMPC 2016, Materials Today: Proceedings4; 2017. pp. 3852–3860.
18. Barzegarian R, Moraveji MK, Aloueyan A. Experimental investigation on heat transfer characteristics and pressure drop of BPHE (brazed plate heat exchanger) using TiO_2–water nanofluid. Exp Thermal Fluid Sci. 2016;74:11–8.
19. Raei B, Shahraki F, Jamialahmadi M, Peyghambarzadeh SM. Experimental study on the heat transfer and flow properties of γ-Al_2O_3/water nanofluid in a double-tube heat exchanger. J Therm Anal Calorim. 2017;127(3):2561–75.
20. Barzegarian R, Aloueyan A, Yousefi T. Thermal performance augmentation using water based Al_2O_3-gamma nanofluid in a horizontal shell and tube heat exchanger under forced circulation. Int Commun Heat Mass Transf. 2017;86:52–9.
21. Bahiraei M, Rahmani R, Yaghoobi A, Khodabandeh E, Mashayekhi R, Amani M. Recent research contributions concerning use of nanofluids in heat exchangers: a critical review. Appl Therm Eng. 2018;133:137–59.
22. Yousefi T, Veysi F, Shojaeizadeh E, Zinadini S. An experimental investigation on the effect of Al_2O_3–HO nanofluid on the efficiency of flat-plate solar collectors. Renew Energy. 2012;39(1):293–8.
23. Khodabandeh E, Safaei MR, Akbari S, Akbari OA, Alrashed AAAA. Application of nanofluid to improve the thermal performance of horizontal spiral coil utilized in solar ponds: geometric study. Renew Energy. 2018;122:1–16.
24. Mahian O, Kianifar A, Kalogirou SA, Pop I, Wongwises S. A review of the applications of nanofluids in solar energy. Int J Heat Mass Transf. 2013;57:582–94.
25. Stalin PMJ, Arjunan TV, Matheswaran MM, et al. J Therm Anal Calorim. 2017. https://doi.org/10.1007/s10973-017-6865-4.
26. Trisaksri V, Wongwises S. Nucleate pool boiling heat transfer of TiO_2-R141b nanofluids. Int J Heat Mass Transf. 2009;52(5–6):1582–8.
27. Bi S, Guo K, Liu Z, Wu J. Performance of a domestic refrigerator using TiO2-R600a nano-refrigerant as working fluid. Energy Convers Manag. 2011;52:733–7.
28. Saidur R, Kazi SN, Hossain MS, Rahman MM, Mohammed HA. A review on the performance of nanoparticles suspended with refrigerants and lubricating oils in refrigeration systems. Renew Sustain Energy Rev. 2011;15:310–23.
29. Celen A, Çebi A, Aktas M, Mahian O, Dalkilic AS, Wongwises S. A review of nanorefrigerants: flow characteristics and applications. Int J Refrig. 2014;44:125–40.
30. Sun B, Yang D. Flow boiling heat transfer characteristics of Nanorefrigerants in horizontal tube. Int J Refrig. 2014;38(1):206–14.
31. Sheikholeslami M, Darzi M, Sadoughi MK. Heat transfer improvement and pressure drop during condensation of refrigerant-based nanofluid; an experimental procedure. Int J Heat Mass Transf. 2018;122:643–50.
32. Leong KY, Saidur R, Kazi SN, Mamun AM. Performance investigation of an automotive car radiator operated with

nanofluid-based coolants (nanofluid as a coolant in a radiator). Appl Therm Eng. 2010;30:2685–92.
33. Peyghambarzadeh SM, Hashemabadi SH, Hoseini SM, Seifi JM. Experimental study of heat transfer enhancement using water/ethylene glycol based nanofluids as a new coolant for car radiators. Int Commun Heat Mass Transf. 2011;38:1283–90.
34. Ali HM, Ali H, Liaquat H, Maqsood HTB, Nadir MA. Experimental investigation of convective heat transfer augmentation for car radiator using ZnO–water nanofluids. Energy. 2015;84:317–24.
35. Ali HM, Arshad W. Thermal performance investigation of staggered and inline pin fin heat sinks using water based rutile and anatase TiO_2 nanofluids. Energy Convers Manag. 2015;106:793.
36. Arshad W, Ali HM. Graphene nanoplatelets nanofluids thermal and hydrodynamic performance on integral fin heat sink. Int J Heat Mass Transf. 2017;107:995–1001.
37. Khoshvaght-Aliabadi M, Hassani SM, Mazloumi SH. Enhancement of laminar forced convection cooling in wavy heat sink with rectangular ribs and Al2O3/water nanofluids. Exp Thermal Fluid Sci. 2017;89:199–210.
38. Khoshvaght-Aliabadi M, Sartipzadeh O, Pazdar S, Sahamiyan M. Experimental and parametric studies on a miniature heat sink with offset-strip pins and Al_2O_3/water nanofluids. Appl Therm Eng. 2017;111:1342–52.
39. Azizi Z, Alamdari A, Malayeri MR. Convective heat transfer of Cu–water nanofluid in a cylindrical microchannel heat sink. Energy Convers Manag. 2015;101:515–24.
40. Azizi Z, Alamdari A, Malayeri MR. Thermal performance and friction factor of a cylindrical microchannel heat sink cooled by Cu-water nanofluid. Appl Therm Eng. 2016;99:970–8.
41. Shamsi MR, Akbari OA, Marzban A, Toghraie D, Mashayekhi R. Increasing heat transfer of non-Newtonian nanofluid in rectangular microchannel with triangular ribs. Physica E Low Dimens Syst Nanostruct. 2017;93:167–78.
42. Rezaei O, Akbari OA, Marzban A, Toghraie D, Pourfattah F, Mashayekhi R. The numerical investigation of heat transfer and pressure drop of turbulent flow in a triangular microchannel. Physica E Low Dimens Syst Nanostruct. 2017;93:179–89.
43. Gravndyan Q, Akbari OA, Toghraie D, Marzban A, Mashayekhi R, Karimi R, Pourfattah F. The effect of aspect ratios of rib on the heat transfer and laminar water/TiO_2 nanofluid flow in a two-dimensional rectangular microchannel. J Mol Liq. 2017;236:254–65.
44. Topuz A, Engin T, Alper Özalp A, et al. J Therm Anal Calorim. 2018;131:2843. https://doi.org/10.1007/s10973-017-6790-6.
45. Toghraie D, Abdollah MMD, Pourfattah F, et al. J Therm Anal Calorim. 2018;131:1757. https://doi.org/10.1007/s10973-017-6624-6.
46. Arabpour A, Karimipour A, Toghraie D, et al. J Therm Anal Calorim. 2018;131:2975. https://doi.org/10.1007/s10973-017-6813-3.
47. Nguyen CT, Roy G, Gauthier C, Galanis N. Heat transfer enhancement using Al_2O_3 -water nanofluid for an electronic liquid cooling system. Appl Therm Eng. 2007;27:1501–6. https://doi.org/10.1016/j.applthermaleng.2006.09.028.
48. Chein R, Chuang J. Experimental microchannel heat sink performance studies using nanofluids. Int J Therm Sci. 2007;46(1):57–66.
49. Roberts NA, Walker DG. Convective performance of nanofluids in commercial electronics cooling systems. Appl Therm Eng. 2010;30:2499–504. https://doi.org/10.1016/j.applthermaleng.2010.06.023.
50. Khodabandeh E, Abbasi A. Performance optimization of water–Al_2O_3 nanofluid flow and heat transfer in trapezoidal cooling microchannel using constructal theory and two phase Eulerian–Lagrangian approach. Powder Technol. 2018;323:103–14.
51. Ho CJ, Wei LC, Li ZW. An experimental investigation of forced convective cooling performance of a microchannel heat sink with Al_2O_3/water nanofluid. Appl Therm Eng. 2010;30(2–3):96–103. https://doi.org/10.1016/j.applthermaleng.2009.07.003.
52. Jang SP, Choi SUS. Cooling performance of a microchannel heat sink with nanofluids. Appl Therm Eng. 2006;26:2457–63. https://doi.org/10.1016/j.applthermaleng.2006.02.036.
53. Kalteh M, Abbassi A, Saffar-Avval M, Frijns A, Darhuber A, Harting J. Experimental and numerical investigation of nanofluid forced convection inside wide microchannel heat sink. Appl Therm Eng. 2012;36:260–8.
54. Byrne MD, Hart RA, da Silva AK. Experimental thermal–hydraulic evaluation of CuO nanofluids in microchannels at various concentrations with and without suspension enhancers. Int J Heat Mass Transf. 2012;55(9–10):2684–91.
55. Moraveji MK, Ardehali RM. CFD modeling (comparing single- and two-phase approach) on thermal performance of Al2O3/water nanofluid in mini-channel heat sink. Int Commun Heat Mass Transf. 2013;44:157–64.
56. Savithiri S, Pattamatta A, Das SK. Scaling analysis for the investigation of slip mechanisms in nanofluids. Nanoscale Res Lett. 2011;6:471.
57. Moraveji MK, Darabi M, Hossein Haddad SM, Davarnejad R. Modeling of convective heat transfer of a nanofluid in the developing region of tube flow with computational fluid dynamics. Int Commun Heat Mass Transf. 2011;38:1291–5. https://doi.org/10.1016/j.icheatmasstransfer.2011.06.011.
58. Moraveji MK, Hejazian M. Modeling of Turbulent forced convective heat transfer and friction factor in a tube for Fe_3O_4 magnetic nanofluid with computational fluid dynamics. Int Commun Heat Mass Transf. 2012;39:1293–6.
59. Sheikholeslami M, Ganji DD. Heat transfer of Cu-water nanofluid flow between parallel plates. Powder Technol. 2013;235:873–9.
60. Chon CH, Kihm KD, Lee SP, Choi SUS. Empirical correlation finding the role of temperature and particle size for nanofluid (Al2O3) thermal conductivity enhancement. Appl Phys Lett. 2005;87(15):153107.
61. Manninen M, Taivassalo V, Kallio S: On the mixture model for multiphase flow. Technical Research Centre of Finland: VTT Publications 288; 1996.
62. Mokhtari Moghari R, Akbarinia A, Shariat M, Talebi F, Laur R. Two phase mixed convection Al2O3–water nanofluid flow in an annulus. Int J Multiph Flow. 2011;37(6):585–95.
63. Wakao N, Kaguei S. Heat and mass transfer in packed beds. New York: Routledge; 1982.
64. Akbari M, Galanis N, Behzadmehr A. Comparative assessment of single and two-phase models for numerical studies of nanofluid turbulent forced convection. Int J Heat Fluid Flow. 2012;37:136–46.